

High-harmonic generation in submicron-thick chirped periodically poled thin-film lithium niobate

LINGZHI PENG,¹  XIAONI LI,¹ LIQIANG LIU,¹ YUANYUAN LIU,¹ YUANYUAN ZHAO,² XUANMING DUAN,² LIHONG HONG,^{1,3,4}  AND ZHIYUAN LI^{1,5}

¹School of Physics and Optoelectronics, South China University of Technology, Guangzhou 510641, China

²Guangdong Provincial Key Laboratory of Optical Fiber Sensing and Communications, Institute of Photonics Technology, Jinan University, Guangzhou 511443, China

³State Key Laboratory of Ultra-intense Laser Science and Technology and CAS Center for Excellence in Ultra-intense Laser Science, Shanghai Institute of Optics and Fine Mechanics, Chinese Academy of Sciences, Shanghai 201800, China

⁴e-mail: honglihong@siom.ac.cn

⁵e-mail: phzyli@scut.edu.cn

Received 6 February 2025; revised 21 April 2025; accepted 23 April 2025; posted 23 April 2025 (Doc. ID 558257); published 1 July 2025

Submicron-thick thin-film lithium niobate (TFLN) has emerged as a promising platform for nonlinear integrated photonics. In this work, we demonstrate the efficient simultaneous generation of broadband 2nd–8th harmonics in chirped periodically poled (CPP) TFLN. This is achieved through the synergistic effects of cascaded $\chi^{(2)}$ nonlinear up-conversion and $\chi^{(3)}$ self-phase modulation, driven by near-infrared femtosecond pulses with a central wavelength of 2100 nm and a pulse energy of 1.2 μJ . Remarkably, the 7th and 8th harmonics extend into the deep ultraviolet (DUV) region, reaching wavelengths as short as 250 nm. The 3rd–8th harmonic spectra seamlessly connect, forming a broadband supercontinuum spanning from the DUV to the visible range (250–800 nm, –25 dB), with an on-chip conversion efficiency of 19% (0.23 μJ). This achievement is attributed to the CPP-TFLN providing multiple broadband reciprocal lattice vector bands, enabling quasi-phase matching for a series of $\chi^{(2)}$ nonlinear processes, including second harmonic generation (SHG), cascaded SHG, and third harmonic generation. Furthermore, we demonstrated the significant role of cascaded $\chi^{(2)}$ phase-mismatched nonlinear processes in high-harmonic generation (HHG). Our work unveils the intricate and diverse nonlinear optical interactions in TFLN, offering a clear path toward efficient on-chip HHG and compact coherent white-light sources extending into the DUV. © 2025 Chinese Laser Press

<https://doi.org/10.1364/PRJ.558257>

1. INTRODUCTION

High-harmonic generation (HHG) is a hallmark phenomenon of extreme nonlinear optics (typically in the non-perturbative regime, beyond the scope of traditional $\chi^{(n)}$ processes). Initially, HHG was demonstrated in atomic gases [1], where high-peak-power ultrafast laser pulses interact with atomic gases and plasmas to generate high-order harmonics extending into the extreme ultraviolet and soft X-ray regions [2–4]. This breakthrough directly advanced attosecond science and led to widespread applications in nanoscale structural imaging [5,6], molecular orbital probing [7,8], and attosecond transient absorption in both solid and gas phases [9,10]. In the past decade, HHG in solids has garnered significant attention due to its ability to enable more compact and efficient ultrafast pulse sources, offering new approaches for probing band structures [11–16].

Although HHG in the non-perturbative regime can produce very high-order harmonics and short-wavelength photons, its conversion efficiency remains inherently low compared to traditional $\chi^{(2)}$ nonlinear optical processes. Furthermore, it requires extremely high peak power densities, making it impractical for chip-scale photonic devices [13]. Since the invention of the laser, $\chi^{(2)}$ nonlinear optical effects, such as second harmonic generation (SHG), sum-frequency generation (SFG), and optical parametric amplification, have been widely employed to extend and expand the frequency range of lasers [17–20]. Cascaded $\chi^{(2)}$ nonlinear up-conversion provides an efficient method for transferring pump laser energy to shorter wavelengths and is another effective strategy for achieving HHG [21–23]. In 2015, we demonstrated HHG up to the 8th order in a single lithium niobate (LN) crystal through broadband quasi-phase matching (QPM) [24]. Subsequently, Hickstein

et al. successfully achieved HHG up to the 13th order in a micron-scale LN waveguide based on the same concept [25].

Recently, thin-film lithium niobate (TFLN) has emerged as a promising ultralow-loss nonlinear integrated photonics platform [26–32]. A wide range of optical applications, including broadband frequency conversion [33–35], supercontinuum generation (SCG) [36–39], frequency comb generation [40–42], and entangled photon pair generation [43–45], have been demonstrated in TFLN-based devices such as waveguides, micro-disks/micro-ring resonators, and nanocavities. However, research on HHG in the perturbative nonlinear optical regime within TFLN remains limited. The primary challenge lies in achieving phase matching for a variety of nonlinear up-conversion processes, such as SHG, cascaded SHG, and SFG, simultaneously. This imposes stringent demands on dispersion engineering and domain engineering in QPM-TFLN waveguides.

In this work, we design and fabricate high-quality, uniform reverse-domain structures in TFLN waveguides. These domain structures provide broadband reciprocal lattice vectors (RLVs), enabling phase matching for a series of cascaded $\chi^{(2)}$ nonlinear up-conversion processes. By leveraging the synergistic effects of $\chi^{(2)}$ and $\chi^{(3)}$ nonlinearities, we demonstrate, for the first time, the efficient simultaneous generation of broadband 2nd–8th

harmonics in a chirped-periodically poled (CPP) TFLN waveguide, pumped by near-infrared femtosecond pulses. Remarkably, we observed deep ultraviolet (DUV) signals well below the intrinsic absorption edge of LN (320–350 nm). The spectra of the 3rd–8th harmonics seamlessly combine to form an octave-spanning supercontinuum covering the DUV-visible range (250–800 nm, –25 dB), with an on-chip conversion efficiency up to 19% (0.23 μJ). Additionally, we discover that effective HHG is not only highly dependent on phase-matched cascaded $\chi^{(2)}$ nonlinear up-conversion processes, but also on the significant role of phase-mismatched cascaded processes. Our work demonstrates the enormous potential of the TFLN platform for high-efficiency HHG, offering a novel pathway for the development of compact, on-chip ultrafast, and short-wavelength coherent light sources.

2. PRINCIPLE

Figure 1(a) illustrates the principle of broadband HHG in a TFLN waveguide utilizing cascaded $\chi^{(2)}$ nonlinear up-conversion and together with $\chi^{(3)}$ self-phase modulation (SPM) processes. The core of this scheme is to achieve phase matching for various three-wave mixing processes, including SHG, cascaded SHG, and SFG over a broadband pumping wavelength range,

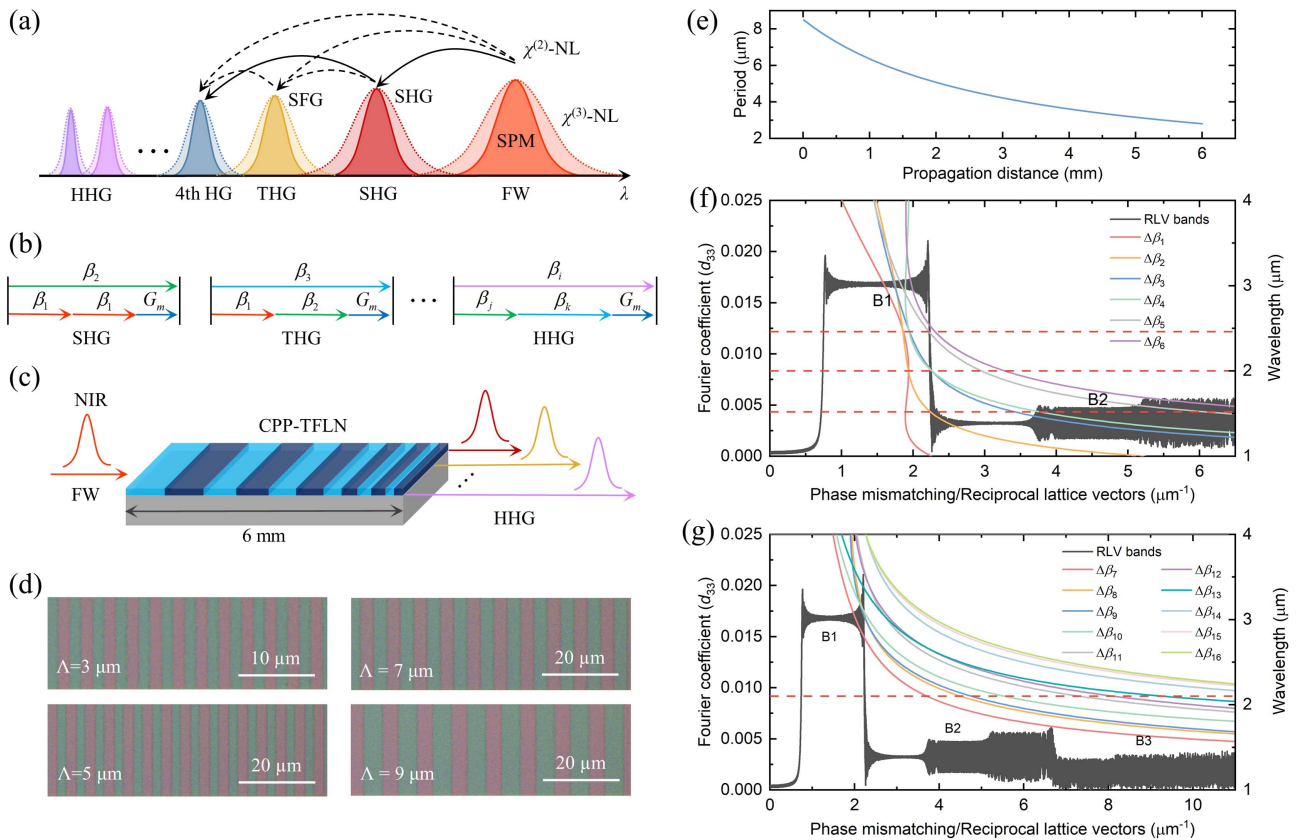


Fig. 1. (a) Schematic of broadband SHG, THG, and HHG via a pumped femtosecond pulse laser under the influence of cascaded $\chi^{(2)}$ nonlinear up-conversion and $\chi^{(3)}$ SPM. (b) Schematic of phase matching for SHG, THG, and HHG through QPM. β_1 and β_i represent the wave vectors of the FW and the i th harmonic, respectively. (c) Schematic of the TFLN waveguide structure used for HHG, with a thickness of 600 nm. (d) Optical microscope image of the poled TFLN surface after hydrofluoric acid etching. The green areas represent the reversed domains. (e) Variation of the TFLN poling period with propagation distance. (f) and (g) Calculated distributions of the d_{eff} as a function of the RLVs for the designed CPP-TFLN waveguide, along with the phase-mismatch curves for each HG during $\chi^{(2)}$ nonlinear up-conversion.

as shown in Fig. 1(b). Among these, phase matching for the generation of low-order harmonics must be prioritized, as it is a prerequisite for the generation of higher-order harmonics. Due to the birefringence effect, mode-phase matching cannot be achieved across such numerous cascaded processes. Therefore, broadband QPM must be introduced in the TFLN waveguide.

Figure 1(c) shows the design of the z -cut CPP-TFLN planar waveguide employed in this study, with a thickness of 600 nm and a length of 6 mm. Along the y -propagation direction, the poling period is modulated according to the formula $\Lambda(y) = \Lambda_0/[1 + (D_c\Lambda_0y/2\pi)]$, where Λ_0 is the initial period and D_c is the chirp rate. An effective nonlinear coefficient model can be used to evaluate the performance of various nonlinear up-conversion in the CPP-TFLN [46,47]. Here we set $\Lambda_0 = 8.7 \mu\text{m}$ and $D_c = 250 \mu\text{m}^{-2}$, ensuring that the poling period gradually decreases from 8.7 μm to 2.8 μm , as shown in Fig. 1(e). Through the use of high-voltage pulse poling techniques and careful optimization of the polarization electrode design, we successfully achieved duty cycles of approximately 50% across different poling periods. Figure 1(d) presents an optical microscope image of the reversed domain structure.

Figures 1(f) and 1(g) display the Fourier transform spectrum of the CPP-TFLN waveguide. The spectrum reveals three important RLV bands: the B1 band, spanning 0.7–2.2 μm^{-1} , the B2 band, spanning 2.2–6.7 μm^{-1} , and the B3 band, which lies beyond 2.2 μm^{-1} . Among these, the B1 band has the largest effective nonlinear coefficient d_{eff} , approximately 0.017 times d_{33} , while the d_{eff} in the other bands are smaller. Notably, although these d_{eff} are much smaller than those in LN, the strong light confinement in TFLN and the high peak power of the pump femtosecond laser still result in significant $\chi^{(2)}$ nonlinear interactions.

To better clarify the QPM mechanism in the designed CPP-TFLN, we present the phase mismatch curves for the generation of 2nd–5th harmonics and the generation of 6th–8th harmonics relative to the pump fundamental wave (FW) in Figs. 1(f) and 1(g), respectively. The wave vector mismatch $\Delta\beta$ for different nonlinear frequency conversion processes responsible for each HG is defined in Table 1. When a specific $\Delta\beta$ is compensated by the appropriate RLV bands G_m (where

$G_m = m2\pi/\Lambda_0$, and m represents the QPM order), effective QPM can be achieved. As shown in Fig. 1(f), the combined effects of the B1 and B2 bands enable the generation of 2nd–5th harmonics over a broad pump wavelength range of 1.5–4 μm . Specifically, the B1 band supports SHG across 1–4 μm , THG across 1.5–4 μm , 4th HG across 2–4 μm , and 5th HG across 2.46–4 μm . The B2 band supports THG across 1–1.5 μm , 4th HG across 1.25–2 μm , and 5th HG across 1.5–2.46 μm , filling the gap left by the B1 band. Similarly, Fig. 1(g) shows that, with the combined effects of the B1–B3 bands, 2nd–8th HG can be achieved across the mid-infrared pump range. Notably, only the interaction between the transverse magnetic (TM) fundamental modes of each harmonic is considered here, as the TM mode can simultaneously utilize the largest nonlinear coefficient d_{33} and the largest mode overlap area, thereby achieving the highest conversion efficiency.

3. EXPERIMENT AND DISCUSSION

The experimental setup is shown in Fig. 2(a). The near-infrared (NIR) pump source is a femtosecond optical parametric amplifier (TOPAS Prime-F, Spectra-Physics), which offers tunable wavelengths. A short-focus calcium fluoride cylindrical lens focuses the pump light into a light sheet, enabling efficient coupling into the TFLN waveguide, which is mounted on a three-dimensional adjustable displacement platform for precise alignment. The output spectrum is recorded using two fiber spectrometers (Maya 2000Pro, 200–1100 nm, and NIR Quest, 900–2500 nm; Ocean Optics). The pump wavelength was set to approximately 2100 nm, with the pump energy fixed at 60 μJ . The coupling efficiency in the experiment was approximately 2%, corresponding to 1.2 μJ of energy coupled into the TFLN waveguide—an impressive value, enabled by the large cross-section of the TFLN waveguide, which tolerates microjoule-level energies without optical damage. Figure 2(b) shows the emitted spot profile at the end of the TFLN waveguide, captured on a screen placed approximately 5 cm from the waveguide facet. The emitted spot profile is symmetrically distributed about the end face of the waveguide, consistent with the characteristics of planar waveguide output. A strong white light in the center is visible to the naked eye, indicating a rich spectral composition in the visible region.

A detailed spectral analysis was conducted using the spectrometers. As shown in Fig. 2(c), the pump pulse undergoes significant spectral broadening during propagation through the TFLN waveguide due to SPM, providing additional frequency components that drive the cascaded $\chi^{(2)}$ nonlinear up-conversion processes. The harmonic spectrum is shown in Fig. 2(d). Five distinct spectral bands were observed within the 320–1100 nm range, with peak wavelengths near 1050 nm, 700 nm, 525 nm, 420 nm, and 350 nm, corresponding to the 2nd–6th harmonics of the FW pump light. Remarkably, the spectra of the 3rd–8th harmonics are nearly gap-free, forming an octave-spanning supercontinuum in the DUV-visible range. Excitingly, DUV signals with wavelengths as short as 250 nm, corresponding to the 7th and 8th harmonics, were detected below the strong absorption edge of LN (320–350 nm). These

Table 1. Wave Vector Mismatch ($\Delta\beta$) for Different $\chi^{(2)}$ Nonlinear Up-Conversion Processes Contributing to Each HG^a

HHG	Phase Mismatching in Three-Wave Mixing Processes
2nd HG	$\Delta\beta_1 = \beta_2 - 2\beta_1$
3rd HG	$\Delta\beta_2 = \beta_3 - \beta_2 - \beta_1$
4th HG	$\Delta\beta_3 = \beta_4 - \beta_3 - \beta_1, \Delta\beta_4 = \beta_4 - 2\beta_2$
5th HG	$\Delta\beta_5 = \beta_5 - \beta_4 - \beta_1, \Delta\beta_6 = \beta_5 - \beta_3 - \beta_2$
6th HG	$\Delta\beta_7 = \beta_6 - \beta_5 - \beta_1, \Delta\beta_8 = \beta_6 - \beta_4 - \beta_2,$ $\Delta\beta_9 = \beta_6 - 2\beta_3$
7th HG	$\Delta\beta_{10} = \beta_7 - \beta_6 - \beta_1, \Delta\beta_{11} = \beta_7 - \beta_5 - \beta_2,$ $\Delta\beta_{12} = \beta_7 - \beta_4 - \beta_3$
8th HG	$\Delta\beta_{13} = \beta_8 - \beta_7 - \beta_1, \Delta\beta_{14} = \beta_8 - \beta_6 - \beta_2,$ $\Delta\beta_{15} = \beta_8 - \beta_5 - \beta_3, \Delta\beta_{16} = \beta_8 - 2\beta_4$

^a β_i represents the wave vector of the i th harmonic.

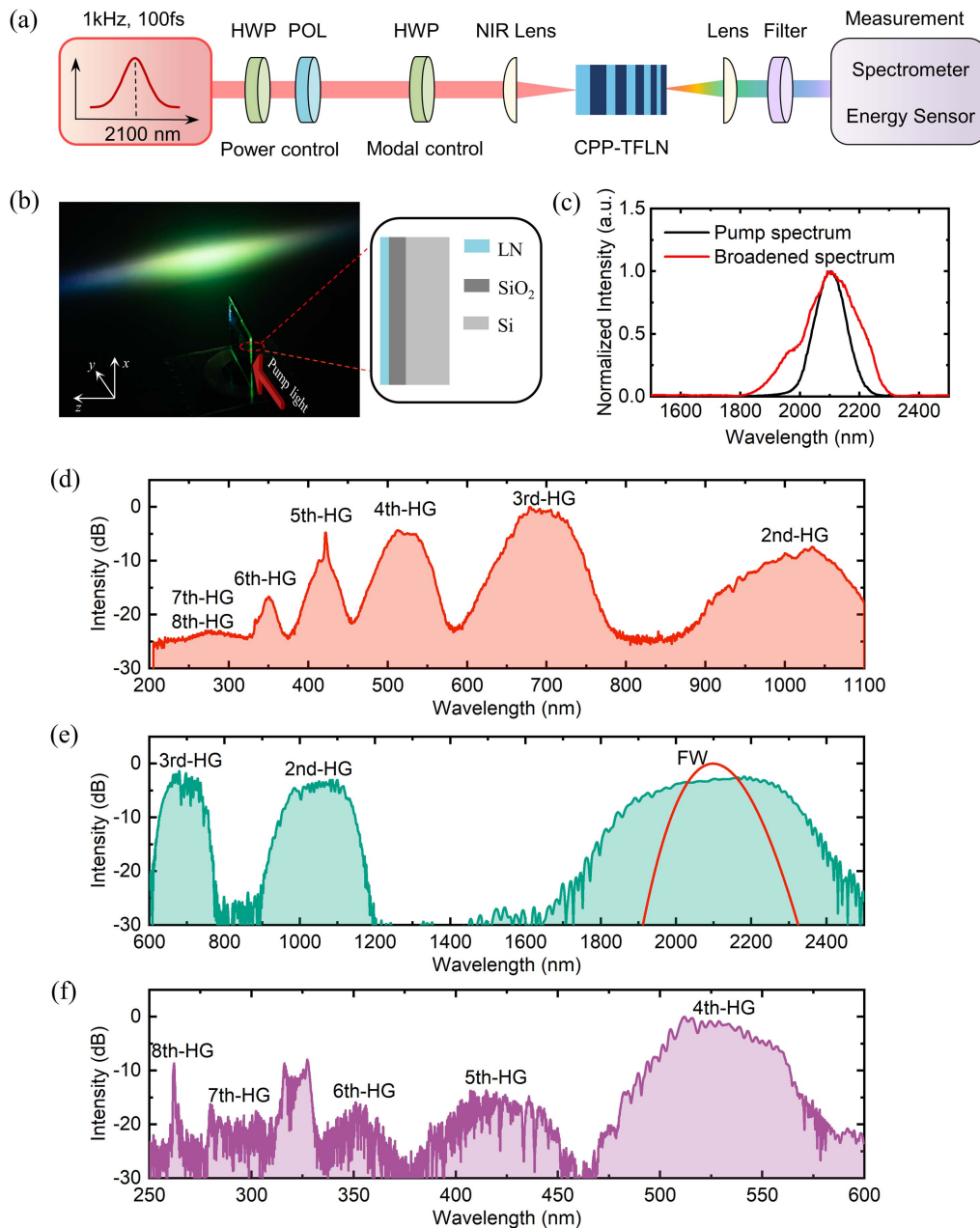


Fig. 2. HHG in the CPP-TFLN waveguide. (a) Schematic of the experimental setup for HHG. HWP, half-wave plate; POL, polarizer. (b) Photograph of the light pattern at the end of the TFLN waveguide. (c) Spectral broadening of the pump laser pulse as it propagates through the TFLN waveguide. (d) Broadband 2nd–8th HG in the TFLN waveguide with a pump energy of 1.2 μJ and a central wavelength of 2100 nm via cascaded $\chi^{(2)}$ nonlinear frequency up-conversion and $\chi^{(3)}$ SPM. (e) and (f) Simulation results of the output spectra. The red curve indicates the initial pump pulse.

represent the shortest wavelengths and highest-order harmonics ever observed on a submicron TFLN waveguide.

The spectral results highlight the critical role of the broadband QPM in the designed CPP-TFLN, validating the RLV band analysis shown in Figs. 1(f) and 1(g). Specifically, across the entire broadband pump range, the phase mismatch curves for SHG ($\Delta\beta_1$), THG ($\Delta\beta_2$), and 4th HG ($\Delta\beta_3, \Delta\beta_4$) overlap with the B1 band. This indicates that all frequency components of the broadband FW can achieve QPM for 2nd–4th HG, ensuring efficient utilization of pump energy. The phase

mismatch curves for 5th HG ($\Delta\beta_5, \Delta\beta_6$) and 6th HG ($\Delta\beta_7, \Delta\beta_8, \Delta\beta_9$) overlap with the B2 band, enabling phase-matching of 5th and 6th HG. Despite the relatively lower d_{eff} of the B2 band, the high conversion efficiency of the 2nd–4th harmonics ensures considerable output for the 5th and 6th harmonics. Similarly, the phase mismatch curves for 7th HG ($\Delta\beta_{10}, \Delta\beta_{11}, \Delta\beta_{12}$) and 8th HG ($\Delta\beta_{13}$) are compensated by the B3 band, enabling the generation of 7th and 8th harmonics.

Surprisingly, although the spectrum of the 7th and 8th harmonics extends beyond the transparency window of LN,

significant spectral signals are still detected. This can be attributed to two factors. The first is the high conversion efficiency of the HHG process. Although LN exhibits strong absorption in the UV region, sufficiently high conversion efficiency can still yield observable signals even after partial attenuation. The second is the short propagation distance of UV signals. It is important to note that our HHG scheme is based on cascaded $\chi^{(2)}$ nonlinear up-conversion. As the pump pulse propagates through the waveguide, lower-order harmonics are generated first and then participate in further cascaded interactions to produce higher-order harmonics. Consequently, the 7th and 8th harmonic signals are predominantly generated near the output facet of the waveguide. This results in a minimal propagation path for these UV components inside the TFLN waveguide, thereby reducing absorption losses and allowing detectable UV output below the material's typical transparency window.

To quantify the conversion efficiency for each harmonic, the output light was spectrally filtered using a bandpass filter and measured with an energy meter. The total energy of the 3rd–8th harmonics (250–800 nm) was measured to be 0.23 μJ , corresponding to an on-chip conversion efficiency of 19%. This is a remarkable efficiency, significantly exceeding typical HHG conversion efficiencies reported in gases and solids. Specifically, the on-chip conversion efficiencies for the 3rd–6th harmonics were 13.79%, 3.98%, 0.9%, and 0.11%, respectively, while the 7th and 8th harmonics exhibited efficiencies of 0.07%. It is worth noting that due to relatively large mode mismatch and Fresnel reflections at the waveguide facets, the overall coupling efficiency was approximately 2%, leading to a total external conversion efficiency of only 0.38%. Nevertheless, the on-chip conversion efficiency serves as a direct indicator of the intrinsic nonlinear frequency conversion capability of the waveguide, which is the primary focus of this study.

The broadband and efficient HHG observed is a result of the synergistic effect of $\chi^{(2)}$ and $\chi^{(3)}$ nonlinearities. When the pump energy and conversion efficiency are sufficiently high, the generated harmonics still have sufficiently high intensity to trigger further SPM and other $\chi^{(3)}$ nonlinear processes, broadening their spectra even further. To better illustrate the critical role of both $\chi^{(2)}$ and $\chi^{(3)}$ nonlinearities in the HHG process, we performed numerical simulations of the spectral evolution of the pump pulse as it propagates through the CPP-TFLN waveguide. The simulation is based on an unidirectional propagation equation that simultaneously includes cascaded $\chi^{(2)}$ and $\chi^{(3)}$ nonlinearities [48]. As shown in Figs. 2(e) and 2(f), the simulation results exhibit good agreement with the experimental results in the spectral features over a wide wavelength range. The broadband FW spectrum, broadened by SPM, and the broadband 2nd–8th harmonic spectra, generated by the combined effects of cascaded $\chi^{(2)}$ nonlinearities and $\chi^{(3)}$ SPM, are clearly visible.

To further elucidate the role of the CPP structure, we measured the output spectrum of another TFLN waveguide with an identical geometric configuration but without any domain structure modulation, under the same pump conditions. As shown in Fig. 3, the output spectrum from this unpoled

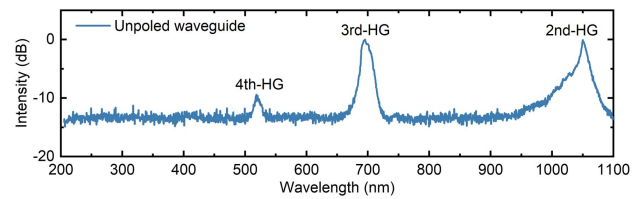


Fig. 3. Output harmonic spectrum in the unpoled TFLN waveguide with a pump energy of 1.2 μJ .

waveguide only exhibits narrowband signals corresponding to phase-mismatched SHG and THG, along with an extremely weak 4th-harmonic component. No harmonic signals beyond the 4th order were observed.

We further measured the output spectra at varying pump energies to illustrate the critical roles of synergistic effect of $\chi^{(2)}$ and $\chi^{(3)}$ nonlinearities in the broadband HHG process. As shown in Fig. 4(a), at low pump energy (0.2 μJ), significant 2nd–5th harmonic signals were generated due to the cascaded $\chi^{(2)}$ nonlinear process. As the pump energy increased, the 6th–8th harmonic signals emerged, with each harmonic's spectrum undergoing significant broadening due to SPM.

To demonstrate the powerful broadband QPM capability of the CPP-TFLN, we measured the output spectra at different

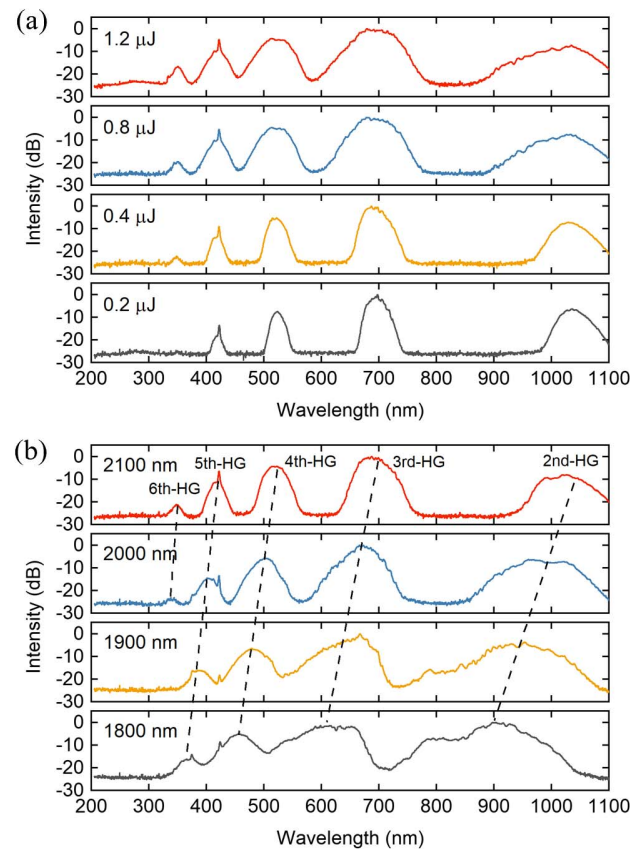


Fig. 4. (a) Output spectra of the TFLN waveguide at varying pump energies. (b) Output spectra at a pump energy of 0.4 μJ for different pump center wavelengths. Note that each spectrum has been normalized to its maximum value.

pump wavelengths, as shown in Fig. 4(b). Significant HHG was observed when the pump center wavelength was varied from 1800 nm to 2100 nm, consistent with theoretical expectations. Notably, compared to longer wavelengths, shorter wavelengths are more tightly confined in the TFLN, resulting in less energy leakage. This enables more efficient HHG and spectral broadening under the same pump energy.

4. FURTHER DISCUSSION

In this section, we systematically analyzed all possible pathways for HHG in the current TFLN system and found that efficient HHG is not only highly dependent on phase-matched cascaded $\chi^{(2)}$ nonlinear up-conversion processes but also significantly influenced by cascaded $\chi^{(2)}$ phase-mismatched nonlinear processes. Effective and broadband HHG is

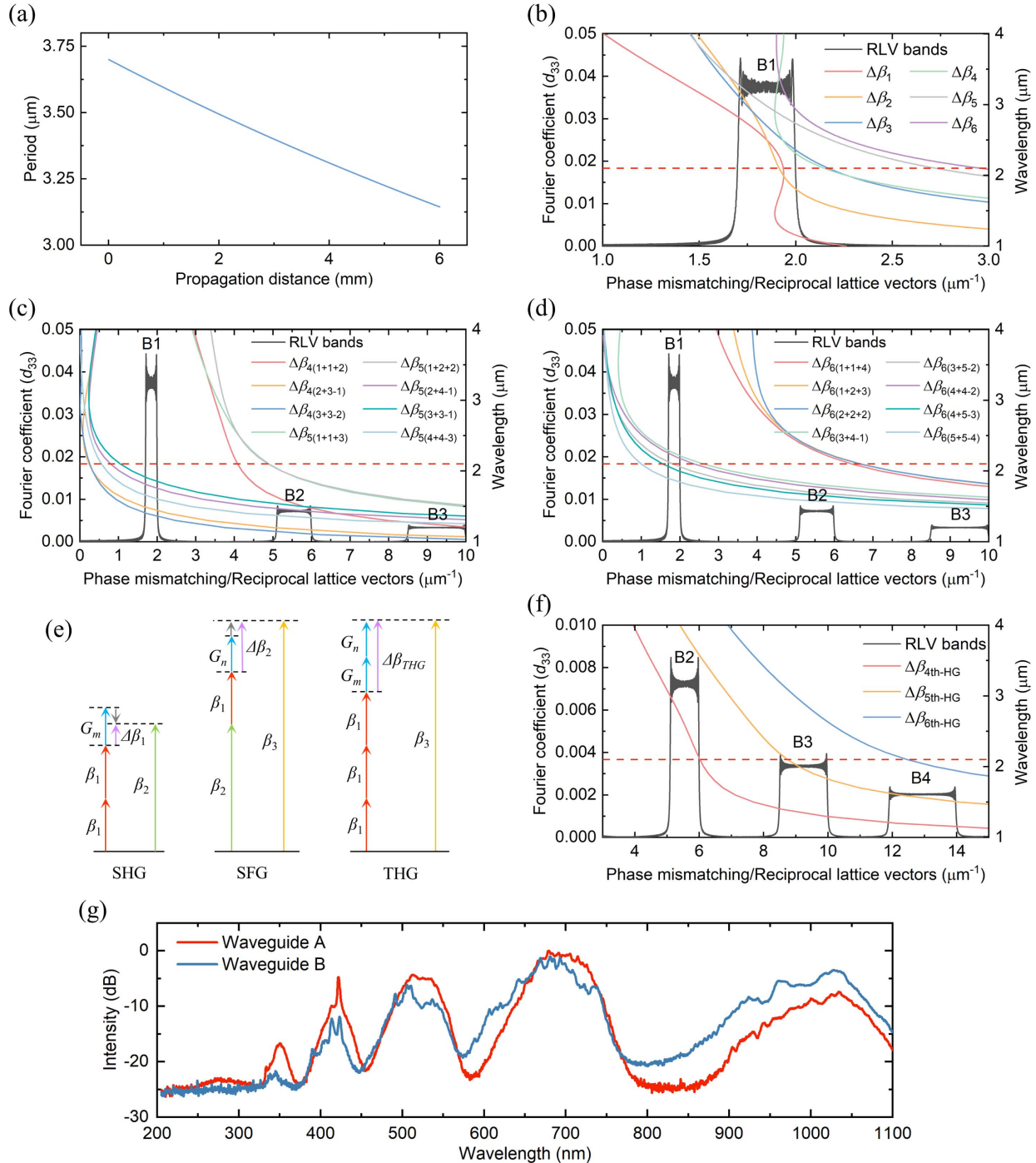


Fig. 5. (a) Variation of the poling period of waveguide B along the propagation direction. (b) The phase-mismatch curves for each HG during the $\chi^{(2)}$ nonlinear up-conversion processes. (c) and (d) The phase-mismatch curves for 4th–6th HG during the $\chi^{(3)}$ FWM processes. (e) Schematic diagram of QPM-THG where individual phase matching conditions for SHG or SFG are not satisfied. The gray arrows indicate phase mismatching. (f) The phase-mismatch curves for the direct 4th–6th HG processes. (g) Output spectrum of the TFLN waveguide with a pump energy of 1.2 μJ and a central wavelength of 2100 nm.

achieved through the synergistic effects of multiple mechanisms.

As shown in Fig. 5(a), we conducted experiments on another CPP-TFLN (waveguide B) with a different domain structure, which provides four distinct RLV bands [Figs. 5(b)–5(d)]. The B1 band only supports SHG and THG for a broadband pump laser with a central wavelength of 2100 nm. Remarkably, significant 4th–6th harmonic signals were observed in the output spectrum [Fig. 5(g)]. This indicates the presence of additional physical mechanisms and energy transfer pathways, in addition to phase-matched cascaded $\chi^{(2)}$ nonlinear up-conversion, that contribute to HHG.

Three possible supplementary mechanisms are considered.

Mechanism 1: Direct-HHG, where the i th harmonic is generated by the absorption of i photons in a single step. However, $\chi^{(4)} - \chi^{(6)}$ are nearly zero, rendering their effects negligible, and such significant 4th–6th HG cannot be attributed to direct-HHG processes.

Mechanism 2: Cascaded $\chi^{(3)}$ nonlinear up-conversion. If the corresponding four-wave mixing (FWM) process can achieve phase matching, effective HHG could be realized under high-peak-power femtosecond pulse pumping. However, as shown in Figs. 5(c) and 5(d), the RLVs of waveguide B cannot effectively compensate for the phase mismatch in the 4th–6th HG processes, thus failing to explain the experimental phenomenon well.

Mechanism 3: Cascaded $\chi^{(2)}$ phase-mismatched nonlinear processes. Previous studies have shown that the generation of intermediate-order harmonics in cascaded $\chi^{(2)}$ nonlinear processes allows for phase mismatches [25,49,50]. Taking THG as an example, even if both the SHG process ($\omega + \omega = 2\omega$, $\Delta\beta_1$) and SFG process ($\omega + 2\omega = 3\omega$, $\Delta\beta_2$) are phase mismatched, effective THG ($\omega + \omega + \omega = 3\omega$, $\Delta\beta_{\text{THG}}$) can still be achieved as long as the direct-THG process is phase-matched [Fig. 5(e)]. In this mechanism, the generation of each harmonic still essentially depends on cascaded $\chi^{(2)}$ nonlinear processes, while phase matching is treated in the same way as direct-HHG. This supplementary mechanism provides a satisfactory explanation for the experimental phenomenon. As shown in Fig. 5(f), the B2–B4 bands of waveguide B compensate for the phase mismatches in direct 4th–6th HG processes, thus enabling efficient generation of 4th–6th harmonics.

It is important to emphasize that phase-matched cascaded $\chi^{(2)}$ nonlinear processes remain the primary factor for achieving efficient HHG, while mechanism 3 mentioned above is the secondary factor that simply provides an additional energy transfer pathway. Therefore, in any case, ensuring efficient SHG must be prioritized in order to achieve effective HHG.

To better illustrate the important influence of phase-matched cascaded $\chi^{(2)}$ nonlinear processes on HHG, we compare the output spectra of the two waveguides. As shown in Fig. 5(g), since the d_{eff} of the B1 band in waveguide B is twice that of waveguide A, more efficient SHG and THG are achieved in waveguide B, resulting in more significant spectral broadening due to SPM. However, the narrow RLV bands of waveguide B fail to fully compensate for the phase mismatch in cascaded $\chi^{(2)}$ nonlinear up-conversion processes, lacking additional energy transfer channels, which ultimately leads to weaker 5th–8th HG.

5. CONCLUSION

In conclusion, we have demonstrated the efficient simultaneous generation of broadband 2nd–8th harmonics in a CPP-TFLN. Notably, the 7th and 8th harmonics extend below the bandgap of LN (3.4–3.9 eV), revealing deep ultraviolet signals as short as 250 nm, representing the shortest wavelength and highest-order harmonics ever observed in a submicron-thick TFLN waveguide. The spectra of the 3rd–8th harmonics seamlessly merge, forming an octave-spanning supercontinuum covering the deep ultraviolet to visible spectrum (250–800 nm, –25 dB), with an on-chip conversion efficiency up to 19% and a pulse energy reaching 0.23 μJ . This achievement is attributed to three key factors. First, the specially designed CPP-TFLN provides broadband RLVs structure, compensating for phase mismatches in the SHG, cascaded SHG, and THG processes, thereby enabling efficient conversion of most of the pump laser energy into high-order harmonics. Second, the cascaded $\chi^{(2)}$ phase-mismatched nonlinear processes serve as additional energy transfer channels, promoting harmonic generation. Third, the strong light confinement in the TFLN significantly enhances the intensity and conversion efficiency of various nonlinear optical interactions, further broadening the generated harmonic spectra through SPM, ultimately forming a gap-free broadband supercontinuum. Our work reveals the complexity and diversity of nonlinear optical interactions, deepening the understanding of the HHG process. It provides valuable insights for achieving efficient on-chip HHG, SCG, and compact short-wavelength coherent light sources.

Funding. National Natural Science Foundation of China (12434016, 11974119); Science and Technology Project of Guangdong (2020B010190001); National Funded Postdoctoral Researcher Program (GZB20240785).

Disclosures. The authors declare no conflicts of interest.

Data Availability. Data underlying the results presented in this paper are not publicly available at this time but may be obtained from the authors upon reasonable request.

REFERENCES

1. M. Ferray, A. L'Huillier, X. F. Li, *et al.*, "Multiple-harmonic conversion of 1064 nm radiation in rare gases," *J. Phys. B At. Mol. Opt. Phys.* **21**, L31 (1988).
2. A. Rundquist, C. G. Durfee, Z. Chang, *et al.*, "Phase-matched generation of coherent soft X-rays," *Science* **280**, 1412–1415 (1998).
3. D. Popmintchev, C. Hernández-García, F. Dollar, *et al.*, "Ultraviolet surprise: efficient soft X-ray high-harmonic generation in multiply ionized plasmas," *Science* **350**, 1225–1231 (2015).
4. N. Y. Joly, J. Nold, W. Chang, *et al.*, "Bright spatially coherent wavelength-tunable deep-UV laser source using an Ar-filled photonic crystal fiber," *Phys. Rev. Lett.* **106**, 203901 (2011).
5. D. F. Gardner, M. Tanksalvala, E. R. Shanblatt, *et al.*, "Subwavelength coherent imaging of periodic samples using a 13.5 nm tabletop high-harmonic light source," *Nat. Photonics* **11**, 259–263 (2017).
6. S. D. C. Abbing Roscam, R. Kolkowski, Z.-Y. Zhang, *et al.*, "Extreme-ultraviolet shaping and imaging by high-harmonic generation from nanostructured silica," *Phys. Rev. Lett.* **128**, 223902 (2022).
7. J. Itatani, J. Levesque, D. Zeidler, *et al.*, "Tomographic imaging of molecular orbitals," *Nature* **432**, 867–871 (2004).

8. B. K. McFarland, J. P. Farrell, P. H. Bucksbaum, *et al.*, "High harmonic generation from multiple orbitals in N₂," *Science* **322**, 1232–1235 (2008).
9. E. Goulielmakis, Z.-H. Loh, A. Wirth, *et al.*, "Real-time observation of valence electron motion," *Nature* **466**, 739–743 (2010).
10. M. Schultze, K. Ramasesha, C. D. Pemmaraju, *et al.*, "Attosecond band-gap dynamics in silicon," *Science* **346**, 1348–1352 (2014).
11. S. Ghimire, A. D. DiChiara, E. Sistrunk, *et al.*, "Observation of high-order harmonic generation in a bulk crystal," *Nat. Phys.* **7**, 138–141 (2010).
12. M. Hohenleutner, F. Langer, O. Schubert, *et al.*, "Real-time observation of interfering crystal electrons in high-harmonic generation," *Nature* **523**, 572–575 (2015).
13. S. Ghimire and D. A. Reis, "High-harmonic generation from solids," *Nat. Phys.* **15**, 10–16 (2018).
14. E. Goulielmakis and T. Brabec, "High harmonic generation in condensed matter," *Nat. Photonics* **16**, 411–421 (2022).
15. P. J. van Essen, Z. Nie, B. Keizerde, *et al.*, "Toward complete all-optical intensity modulation of high-harmonic generation from solids," *ACS Photonics* **11**, 1832–1843 (2024).
16. S. Han, H. Kim, Y. W. Kim, *et al.*, "High-harmonic generation by field enhanced femtosecond pulses in metal-sapphire nanostructure," *Nat. Commun.* **7**, 13105 (2016).
17. R. W. Boyd, A. L. Gaeta, and E. Giese, in *Springer Handbook of Atomic, Molecular, and Optical Physics* (Springer, 2008), pp. 1097–1110.
18. G. P. Agrawal, "Nonlinear fiber optics," in *Nonlinear Science at the Dawn of the 21st Century* (Springer Nature, 2000), pp. 195–211.
19. S.-N. Zhu, Y.-Y. Zhu, and N.-B. Ming, "Quasi-phase-matched third-harmonic generation in a quasi-periodic optical superlattice," *Science* **278**, 843–846 (1997).
20. B.-Q. Chen, M.-L. Ren, R.-J. Liu, *et al.*, "Simultaneous broadband generation of second and third harmonics from chirped nonlinear photonic crystals," *Light Sci. Appl.* **3**, e189 (2014).
21. L. Hong, C. Hu, Y. Liu, *et al.*, "350–2500 nm supercontinuum white laser enabled by synergic high-harmonic generation and self-phase modulation," *Photonix* **4**, 11 (2023).
22. L. Hong, L. Liu, Y. Liu, *et al.*, "Intense ultraviolet-visible-infrared full-spectrum laser," *Light Sci. Appl.* **12**, 199 (2023).
23. S. Liu, Y. Zheng, and X. Chen, "Cascading second-order nonlinear processes in a lithium niobate-on-insulator microdisk," *Opt. Lett.* **42**, 3626–3629 (2017).
24. B.-Q. Chen, C. Zhang, C.-Y. Hu, *et al.*, "High-efficiency broadband high-harmonic generation from a single quasi-phase-matching nonlinear crystal," *Phys. Rev. Lett.* **115**, 083902 (2015).
25. D. D. Hickstein, D. R. Carlson, A. Kowligy, *et al.*, "High-harmonic generation in periodically poled waveguides," *Optica* **4**, 1538–1544 (2017).
26. G. Chen, N. Li, J. D. Ng, *et al.*, "Advances in lithium niobate photonics: development status and perspectives," *Adv. Photonics* **4**, 034003 (2022).
27. A. Boes, L. Chang, C. Langrock, *et al.*, "Lithium niobate photonics: unlocking the electromagnetic spectrum," *Science* **379**, eabj4396 (2023).
28. D. Sun, Y. Zhang, D. Wang, *et al.*, "Microstructure and domain engineering of lithium niobate crystal films for integrated photonic applications," *Light Sci. Appl.* **9**, 197 (2020).
29. A. Boes, B. Corcoran, L. Chang, *et al.*, "Status and potential of lithium niobate on insulator (LNOI) for photonic integrated circuits," *Laser Photonics Rev.* **12**, 1700256 (2018).
30. Y. Zheng and X. Chen, "Nonlinear wave mixing in lithium niobate thin film," *Adv. Phys. X* **6**, 1889402 (2021).
31. M. G. Vazimali and S. Fathpour, "Applications of thin-film lithium niobate in nonlinear integrated photonics," *Adv. Photonics* **4**, 034001 (2022).
32. A. Honardoost, K. Abdelsalam, and S. Fathpour, "Rejuvenating a versatile photonic material: thin-film lithium niobate," *Laser Photonics Rev.* **14**, 2000088 (2020).
33. J. Mishra, M. Jankowski, A. Y. Hwang, *et al.*, "Ultra-broadband mid-infrared generation in dispersion-engineered thin-film lithium niobate," *Opt. Express* **30**, 32752–32760 (2022).
34. M. Jankowski, C. Langrock, B. Desiatov, *et al.*, "Ultrabroadband nonlinear optics in nanophotonic periodically poled lithium niobate waveguides," *Optica* **7**, 40–46 (2020).
35. L. Peng, L. Liu, X. Li, *et al.*, "Efficient simultaneous second harmonic generation and dispersive wave generation in lithium niobate thin film," *Laser Photonics Rev.* **19**, 2400335 (2024).
36. T.-H. Wu, L. Ledezma, C. Fredrick, *et al.*, "Visible-to-ultraviolet frequency comb generation in lithium niobate nanophotonic waveguides," *Nat. Photonics* **18**, 218–223 (2024).
37. M. Ludwig, F. Ayhan, T. M. Schmidt, *et al.*, "Ultraviolet astronomical spectrograph calibration with laser frequency combs from nanophotonic lithium niobate waveguides," *Nat. Commun.* **15**, 7614 (2024).
38. M. Yu, B. Desiatov, Y. Okawachi, *et al.*, "Coherent two-octave-spanning supercontinuum generation in lithium-niobate waveguides," *Opt. Lett.* **44**, 1222–1225 (2019).
39. J. Lu, J. B. Surya, X. Liu, *et al.*, "Octave-spanning supercontinuum generation in nanoscale lithium niobate waveguides," *Opt. Lett.* **44**, 1492–1495 (2019).
40. M. Zhang, B. Buscaino, C. Wang, *et al.*, "Broadband electro-optic frequency comb generation in a lithium niobate microring resonator," *Nature* **568**, 373–377 (2019).
41. C. Tang, M. Nie, J. Y. Chen, *et al.*, "Broadband frequency comb generation through cascaded quadratic nonlinearity in thin-film lithium niobate microresonators," *Opt. Lett.* **49**, 2449–2452 (2024).
42. Y. Okawachi, M. Yu, B. Desiatov, *et al.*, "Chip-based self-referencing using integrated lithium niobate waveguides," *Optica* **7**, 702–707 (2020).
43. J. Zhao, C. Ma, M. Rusing, *et al.*, "High quality entangled photon pair generation in periodically poled thin-film lithium niobate waveguides," *Phys. Rev. Lett.* **124**, 163603 (2020).
44. X. Shi, S. S. Mohanraj, V. Dhyani, *et al.*, "Efficient photon-pair generation in layer-poled lithium niobate nanophotonic waveguides," *Light Sci. Appl.* **13**, 282 (2024).
45. J. Liu, J. Duan, P. Zhu, *et al.*, "Modal phase-matching in thin-film lithium niobate waveguides for efficient generation of entangled photon pairs," *Opt. Express* **32**, 40629–40639 (2024).
46. C.-Y. Hu and Z.-Y. Li, "An effective nonlinear susceptibility model for general three-wave mixing in quasi-phase-matching structure," *J. Appl. Phys.* **121**, 123110 (2017).
47. L. Peng, L. Hong, and Z. Li, "Theoretical solution of second-harmonic generation in periodically poled lithium niobate and chirped periodically poled lithium niobate thin film via quasi-phase-matching," *Phys. Rev. A* **104**, 053503 (2021).
48. T. Voumard, M. Ludwig, T. Wildi, *et al.*, "Simulating supercontinua from mixed and cascaded nonlinearities," *APL Photonics* **8**, 036114 (2023).
49. S. K. Das, S. Mukhopadhyay, N. Sinha, *et al.*, "Direct third harmonic generation due to quadratic cascaded processes in periodically poled crystals," *Opt. Commun.* **262**, 108–113 (2006).
50. J. C. Delagnes, K. L. Vodopyanov, and L. Canioni, "Third harmonic generation in periodically poled crystals," *Proc SPIE* **7917**, 79171C (2011).